Diffuse-scattering-informed Geometric Channel Modeling for THz Wireless Communications Systems

Leyre Azpilicueta, *Senior Member, IEEE*, Alper Schultze, *Member, IEEE*, Mikel Celaya-Echarri, *Member, IEEE*, Fidel A. Rodríguez-Corbo, Costas Constantinou, *Senior Member, IEEE*, Raed. M. Shubair, *Senior Member, IEEE*, Francisco Falcone, *Senior Member, IEEE*, and Miguel Navarro-Cía, *Senior Member, IEEE*

***Abstract*—Surpassing 100 Gbps data throughput is a key objective and an active area of research for sixth-generation (6G) wireless networks that can only be met by exploiting the TeraHertz (THz) frequency band (0.3 - 10 THz). THz channel modeling faces new challenges given the emerging relevance of scattering and molecular absorption in this frequency range as well as the lack of a reliable library of material properties. In this work, we address these challenges by measuring systematically the dielectric properties of 27 common building and office materials and reporting an in-house three-dimensional ray-launching (3D-RL) algorithm that uses the created material library and accounts for rough surface scattering and atmospheric attenuation. In order to validate the proposed algorithm, a channel sounder measurement campaign has been performed in a typical indoor environment at 300 GHz. Simulations and measurements show good agreement, demonstrating the need for modelling scattering and atmospheric absorption in the THz band. The proposed channel model approach enables scenarios at THz frequencies to be investigated by simulation, providing a relevant knowledge for the development of ultra-high-speed wireless communication systems.**

***Index Terms*—TeraHertz (THz), channel modeling, ray-launching, 6G, channel measurements, wireless communications, diffuse scattering.**

This work was supported in part by the Royal Society [Grant No. IES\R3\183131], in part by the Engineering and Physical Sciences Research Council (EPSRC) [Grant Nos. EP/S018395/1 and EP/X014118/1], and in part by MCIN/AEI/10.13039/501100011033 and NextGenerationEU/PRTR [Grant Nos. RYC2021-031949-I and PID2021-127409OB-C31]. For the purpose of open access, the authors have applied a Creative Commons Attribution (CC BY) license to any accepted manuscript version arising. (*Corresponding author: Leyre Azpilicueta*)

L. Azpilicueta and F. Falcone are with the Department of Electrical, Electronic and Communication Engineering and the Institute of Smart Cities, Public University of Navarre (UPNA), 31006, Pamplona, Spain. (e-mail: leyre.azpilicueta@unavarra.es)

A. Schultze is with the Fraunhofer Institute for Telecommunications, Heinrich Hertz Institute, HHI, Berlin, Germany (e-mail: alper.schultze@hhi.fraunhofer.de).

M. Celaya-Echarri is with the Department of Statistics, Computer Science and Mathematics, Public University of Navarre (UPNA), 31006, Pamplona, Spain (e-mail: mikel.celaya@unavarra.es).

C. Constantinou is with the Department of Electronic, Electrical and System Engineering, University of Birmingham, Birmingham B15 2TT, United Kingdom.

Raed. M. Shubair is with the New York University Abu Dhabi, Abu Dhabi 129188, UAE.

F. A. Rodríguez-Corbo and F. Falcone are with the School of Engineering and Sciences, Tecnologico de Monterrey, Mexico.

M. Navarro-Cía is with the School of Physics and Astronomy, and the Department of Electronic, Electrical and System Engineering, University of Birmingham, Birmingham B15 2TT, United Kingdom (e-mail: M.Navarro-Cia@bham.ac.uk).

Manuscript received March XX, 2023; revised XX YY, 2023.

I. Introduction

THE sixth generation (6G) of wireless communication systems is envisioned to use the TeraHertz (THz) communication spectrum [1]. The THz band is located between the microwave and infrared ranges of the electromagnetic spectrum, spanning from 0.3 THz to 10 THz, with wavelengths ranging from 1 mm to 0.03 mm [2]. Recently, it has attracted special attention for its potential applications such as sensing, spectroscopy and imaging, communications (including wireless cognition - the concept of providing a communication link that enables massive computations to be conducted remotely from the device that is doing real-time actions), and localization/positioning, with the advantages of ultra-high and fast data transmission, very low latencies, large bandwidth and transparency through many optically opaque materials [3]. Even with state-of-the-art THz devices [4], any foreseen application will struggle to deliver the expected impact due to the lack of knowledge of propagation channels. Although methodologies of channel modelling for the THz band can be inherited from those in the millimeter wave (mmWave) band, a specific modelling and parameterization of THz channels is still required in order to accurately characterize THz wave propagation for diverse 6G application scenarios [1]; the smaller wavelength is comparable to the size of dust, rain, snow, and roughness of walls. Thus, THz waves interact through reflection, scattering and diffraction with smaller environmental structures, such as surface roughness with sub-millimeter dimensions, and suffer from absorption and scattering by molecules and tiny particles in the atmosphere. They exhibit unique behaviors compared with mmWaves, microwaves and radio waves for which propagation and channel models are well established.

A. THz Channel Modelling State-of-the-Art

The different methodologies to perform the physical wireless channel modeling can be broadly classified as stochastic/statistical, deterministic and hybrid approaches [3]. Stochastic/statistical methods use random distributions and processes to model the channel parameters. They are predominantly based on measurements and describe general types of environments rather than site-specific locations. Their advantages are the low computational complexity and high adaptability, at the expense of low accuracy. The work in [5] presents a stochastic model for a kiosk downloading

TABLE I: Current channel modeling approaches for THz frequency bands.

Ref.	Type	Model approach	Scattering from rough surfaces analysis	Material properties / Measurement method	Freq. (GHz)	Scenario complexity	Model validation / Measurement method	Channel metrics
[5]	Model	Stochastic	-	Calibrated from the performed channel measurements / -	220-340	Kiosk downloading communication system	RT results / VNA channel measurement campaign	Power, RMS delay spread and Rician k-factor.
[6]	Model	Stochastic	Separate stochastic scattering model [7]	Calibrated, considered from [8] / -	275-325	Typical office room	RT results / -	Ray amplitudes, times of arrival, angles of arrival and departures, path specific frequency dispersion.
[9]	Model	Stochastic	Kirchoff theory	- / -	300-350	Typical indoor scenario	Measurements from the literature [8], [10] / -	Non-stationary ultra-massive MIMO model. Statistical properties: space-time-frequency correlation function.
[11]	Model	RT	Kirchoff theory	Considered from the literature [12] / -	300	Simple office room	Measurements from the literature [12] / -	Coherence bandwidth, RMS delay spread, wideband channel capacity.
[12]	Model	RT	Kirchoff theory	Measured / Fiber-coupled THz time-domain spectroscopy system	300	Simple office room	- / -	Diffuse scattering implication on channel modeling.
[8]	Charact. / Model	RT	Kirchoff theory	Calibrated from the performed channel measurements / -	275-325	Typical office room	Measurements / VNA channel measurement campaign	Angular power spectrum, time of arrival, power delay profiles, k-factor, RMS delay spread.
[13]	Model	RT	Kirchoff approximation	Considered from the literature [12] / -	350	Typical office room	- / -	Angular power spectrum, time of arrival, power delay profile.
[14]	Charact. / Model	RT	Scattering patterns from [15]	Calibrated, considered from [16] / -	300	Urban and highway scenarios	Measurements from the literature [16] / Correlation-based channel sounder	Path loss, Rician k-factor, RMS delay spread, and angular spreads under different weather conditions.
[17]	Model	Hybrid: Commercial RT/Diffuse scattering algorithm	Kirchoff theory	Considered from the literature [18]–[20] / -	300	Typical office room	- / -	Channel capacity with multiple-antenna configurations with three different surface types of wall and ceiling.
This work	Charact. / Model	RT	Kirchoff theory	Measured / THz time-domain spectroscopy system	300	Typical office scenario	Measurements / Time-domain channel sounding	Path loss, RMS delay spread and angular spread.

communication system. The model is developed using a vector network analyzer (VNA) channel measurement campaign in an anechoic chamber at the 220 to 340 GHz frequency band. The electromagnetic properties of the considered materials in the algorithm are inferred from the comparison between ray-tracing simulations and measurements. Ref. [6] presents a stochastic model for a typical office room at the 275 to 325 GHz frequency band, where the scattering model is presented separately in [7]. In addition, the work in [9] presents a stochastic model for non-stationary ultra-massive MIMO channel for a typical office environment at the 300 to 350 GHz frequency band.

Deterministic channel approaches model the wave propagation based on Maxwell's equations or approximations of them, such as finite-difference time-domain (FDTD) methods [21]–[23] or ray tracing/ray launching (RT/RL) methods [11], [24]–[26], respectively. The advantage of these methodologies is the high accuracy they can achieve, but they require detailed information about the geometry of the environment and the electromagnetic properties of all the materials of the considered scenario; the latter requirement is rather challenging at THz frequencies given the lack of a reliable comprehensive material database. In addition, the computational complexity can be prohibitively high depending of the scenario under analysis, especially in deterministic full-wave methods such as FDTD. For this reason, RT techniques have been considered as the most suitable approach for modeling the wireless channel in the THz band, due to their capacity to analyze a large variety of scenarios achieving a trade-off between precision and reasonable computational resources. Although

the assessment of the effects of building material properties and structures on radio wave propagation is recommended in [27] up to 100 GHz, the cost, complexity and time-consuming measurements in the THz spectrum have led to a scarcity of tabulated electromagnetic properties of different materials in this spectral window, impeding the developing of THz deterministic models for urban (indoor and outdoor) environments.

In this context, the work in [12] presents a RT model where the analysis of diffuse scattering on channel modeling at 300 GHz is shown. The Kirchoff approximation is verified with an experimental study of diffuse scattering, using a fiber-coupled THz time-domain spectroscopy system. Electromagnetic material properties of plaster and wallpaper are presented for the THz frequency band. Other work in the literature, such as [11], [13], present a RT model approach for 300 GHz and 350 GHz frequency band, respectively. They use the Kirchoff approximation to model scattering from rough surfaces, and consider the electromagnetic material properties presented in [12] to assess THz signal propagation characteristics in a simple typical office room. The work presented in [8], [14] present a RT model where the electromagnetic material properties of the scenario under analysis are calibrated from experimental measurements. In [8], a typical office room is analyzed at 275 to 325 GHz frequency band, using a VNA channel measurement campaign to calibrate the electromagnetic material properties and validate the RT model. The Kirchoff approximation is used in the RT model to consider scattering from rough surfaces. The work in [14] presents a RT model for the analysis of urban and highway scenarios at 300 GHz frequency band, using an ultra-wideband (UWB) correlation-based channel sounder to calibrate the material properties and validate results; the RT model considers the scattering patterns reported at microwave frequencies in [15].

A summary of the main characteristics of the aforementioned channel models is presented in Table I, for the 300 GHz frequency band. The objective of the Table is to compare the different models in terms of rough surface scattering analysis, THz material characterization technique and channel model validation. The Table presents a non-exhaustive state-of-the-art; the reader can find such exhaustive literature review in two recent surveys on measurement techniques, channel modeling, and analysis of THz wireless channels [2], [3]. It is worthy to mention that most of the aforementioned models consider the electromagnetic material properties calibrated from channel measurements in specific environments, which cannot be generalized. Consequently, in order to have a general material data library to obtain an accurate and trustworthy deterministic channel model, it is important to precisely consider the frequency-dependent electromagnetic material properties at THz bands for all the obstacles in the environment. Thus, further studies are needed, especially in supporting deterministic channel modeling in THz frequency bands.

B. Contribution of present work

This work is motivated by the need to provide and validate an accurate deterministic channel model approach in the THz frequency band. Therefore, with the aim to fill this gap, we present a new add-on THz module for an in-house deterministic three-dimensional ray launching (3D-RL) algorithm. This module includes a THz electromagnetic material properties library created from transmission and reflection measurements of 27 common building and office materials, and it incorporates scattering from rough surfaces and atmospheric attenuation at this frequency band. The THz 3D-RL propagation algorithm is validated in an indoor typical office environment at the 300 GHz frequency band, showing good agreement.

II. THz Materials Characterization

To build up the library of material properties, we rely on a time-domain-based retrieval methodology well established in the literature [28] that we validated and used in previous studies [29], [30]. For this work, we use the Menlo Systems TERA K15 Mark II time-domain spectrometer in collimated normal-incidence transmission and reflection modes without any purging [31], [32] (see Fig. 1). The former mode of operation is used for samples with good transmission, whereas we resort into reflection mode for highly absorbing samples. The temporal length of the waveforms is 143 and 29 ps for transmission and reflection mode, respectively, which corresponds to a spectral resolution of 7 and 34 GHz, respectively. The temporal window for reflection measurements is shortened to not record the Fabry-Perot etalons from the 1 mm thick high resistivity float zone Silicon beam splitter. A time constant of 100 ms is used for the lock-in amplification.

Samples are procured from local DIY and home improvement retailing companies. Rough surface samples are polished prior to the experiments with a 240-grit sandpaper to reduce losses due to scattering and therefore neglect them subsequently in the retrieval method. For transmission measurements, each sample is measured four times with the sample reoriented each time so the average response of the material is determined along with the associated standard error. For reflection measurements, each sample is measured only once. The material properties extraction from transmission measurements is done with the commercial software TeraLyzer [28]. The core of TeraLyzer is a Nelder-Mead simplex algorithm that minimizes the difference between the measured and theoretical complex transfer functions using as a parameter space the thickness and frequency-dependent complex refractive index of the sample. The material properties extraction algorithm for reflection measurements is based on an in-house singly substrative Kramers-Kronig relation methodology detailed in [33].

Table II shows the material properties for 27 common building and office materials at 300 GHz obtained following the measurement and retrieval methodology explained above. Values reported here are consistent with those reported by other authors using board-band Fourier transform [34], [35], broad-band time-domain [19], [36], [37] and narrow-band continuous-wave techniques [35]. The dielectric constant ε_r and loss tangent $\tan(\delta)$ of a subset of these 27 materials up to 1 THz can be found in Ref. [32].

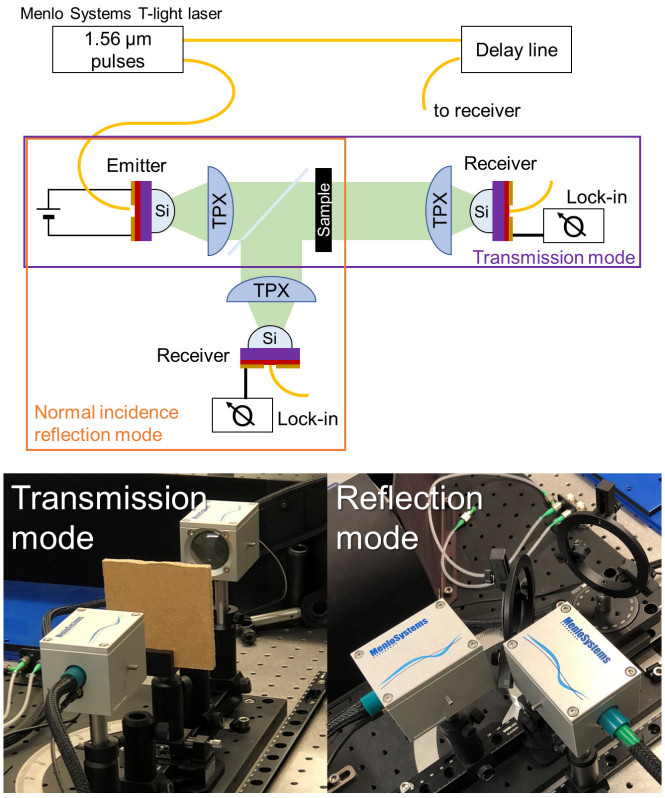

Fig. 1: Top: schematic of the quasi-optical setup. Bottom: picture of the transmission (left) and reflection mode configuration (right).

TABLE II: Measured dielectric properties of selected building and office materials at 300 GHz.

Material	ε_r	tan(δ)	α (cm^{-1})
Transmission measurements			
Aniline Leather	1.771 ± 0.019	0.039 ± 0.0007	3.3
Antique pine	2.148 ± 0.008	0.110 ± 0.001	10.1
Balsa	1.527 ± 0.062	0.044 ± 0.009	3.4
Bamboo	1.772 ± 0.644	0.006 ± 0.004	0.5
Ceramic (green)	3.873 ± 0.009	0.0262 ± 0.0003	3.2
Ceramic (grey)	2.788 ± 0.037	0.0125 ± 0.0002	1.3
Ceramic (white)	3.042 ± 0.004	0.0271 ± 0.0004	3.0
Ceramic tile	3.806 ± 0.020	0.0072 ± 0.0003	0.9
Clear cast acrylic	2.608 ± 0.002	0.021 ± 0.001	2.1
Glass	3.956 ± 0.001	0.067 ± 0.001	8.4
Lever arch file (Blue)	1.975 ± 0.017	0.0370 ± 0.0005	3.3
Lever arch file (Red)	2.234 ± 0.003	0.0443 ± 0.0002	4.2
Lever arch file (Yellow)	2.276 ± 0.023	0.0411 ± 0.0010	3.9
Medium-density fiberboard	2.362 ± 0.008	0.0615 ± 0.0008	5.9
Plywood	2.037 ± 0.040	0.059 ± 0.002	5.3
Polyester (charcoal)	2.706 ± 0.005	0.0215 ± 0.0003	2.2
Polypropylene	2.319 ± 0.003	0.0008 ± 0.0004	0.1
Polystyrene (Jewel case)	2.253 ± 0.008	0.0097 ± 0.0003	0.9
Pressed linen	2.460 ± 0.012	0.0797 ± 0.0009	7.9
Riven slate	6.525 ± 0.021	0.0308 ± 0.0005	4.9
Styrofoam	1.496 ± 0.007	0.0032 ± 0.0008	0.2
Reflection measurements			
Brick	4.478	0.135	17.9
Chipboard	1.453	0.058	4.4
Roof tile	2.218	0.217	20.2
Slate	6.300	0.078	12.3
Stone tile	4.789	0.044	6.1
Unplasticized polyvinyl chloride	1.523	0.017	1.3

III. THz Channel Modeling

A. The Ray Launching Technique

The THz 3D-RL algorithm is based on Geometrical Optics (GO) and the Uniform Theory of Diffraction (UTD), where a set of rays is transmitted following a predefined azimuth/elevation angular distribution combination emulating the antenna radiation pattern. A grid is defined in the space, and specific parameters of each ray along its path are stored in a 3D matrix, considering the ray changing of direction due to reflection, refraction and diffraction until the ray either leaves the area of interest, or the number of rebounds reaches a predetermined threshold.

The in-house developed 3D-RL simulation tool is based on a modular structure to provide full interoperable capabilities within the code. Hence, depending on the frequency under analysis, the microwave, mmWave or THz module analysis developed and presented here is used in the simulation. Each frequency module employs a corresponding electromagnetic materials data library. The algorithm has been widely used and validated with real measurements for different applications below 6 GHz [38]–[42] and mmWave frequency bands [43]–[46]. Here, the THz data library, whose values for 300 GHz are tabulated in the previous section, has been integrated in the 3D-RL algorithm, allowing the assessment of radio wave propagation on site-specific 3D environments up to 1 THz. A schematic view of the implemented THz module with its main distinguishing characteristics is shown in Fig. 2. The main disctintive particularities of the THz module analysis within the 3D-RL package is the consideration of the measured THz material properties data library at the frequency under analysis. In addition to this, electromagnetic phenomena such as reflection, refraction and diffraction are taken into account, as well as scattering from rough surfaces and atmospheric attenuation, which can be relevant at THz frequencies. The different hybrid methodologies implemented in the software are also presented in Fig. 2 for completeness, although they have not been used here; namely the combination of Ray Launching - Neural Network [25], where a lower number of launched rays in the simulation scenario can be used whereas intermediate points are predicted using neural network; Ray Launching - Diffusion Equation [26], [47], where the 3D-RL algorithm is combined with a diffusion equation method based on the equation of transfer; or Ray Launching - Collaborative Filtering [48], [49], where database learning techniques are applied to lessen the poor-quality results of low-definition simulations. These acceleration techniques manage to obtain accurate results with lower simulation times. A decrease in computational cost of up to 80%, 40% and 25%, respectively, can be achieved using these acceleration techniques, while maintaining similar accuracy [25], [26], [49]. The details and validation of the code have been covered in the cited

publications [25], [26], [47]–[49]. Hence, they are not repeated here in the interests of brevity. The 3D-RL package allows enabling or disabling these techniques depending on the results analysis of interest.

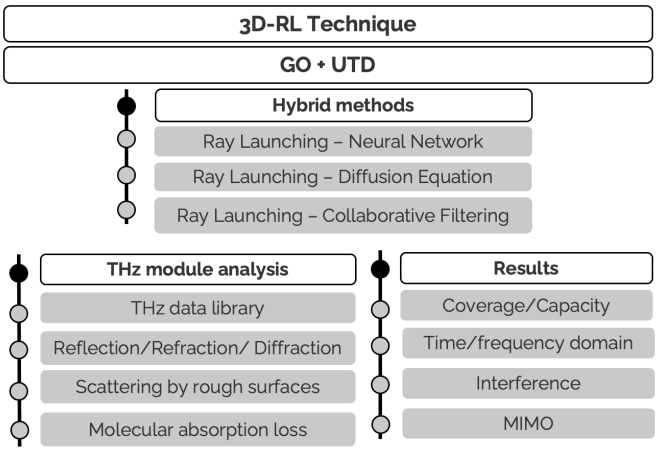

Fig. 2: Schematic view of the implemented THz module analysis integrated in the in-house developed 3D-RL algorithm.

Due to the shorter wavelength as the operation frequency increases, surfaces that are considered smooth for frequencies below 6 GHz, become slightly-to-moderately rough surfaces at mmWaves and moderately-to-very rough at THz frequencies as defined by the literature [50]. An example of the implication of these roughness categories in the automotive radar context can be found in Ref. [30]. Hence, it is important to consider diffuse scattering of the electromagnetic waves, which results in a loss of intensity in the specular direction, as well as multipath propagation. As previously stated, the algorithm is based in the GO approximation combined with UTD, in three-dimensional approach, supported by Fresnel equations to model the transmitted and reflected waves. The proposed THz 3D-RL algorithm considers scattering losses in the specular direction following Rayleigh-Rice theory whereby the Fresnel reflection coefficients for transverse electric (TE) and transverse magnetic (TM) polarized waves, $\Gamma_{smooth}^{TE/TM}$, are multiplied by the Rayleigh roughness factor [51] as follows:

$$\Gamma_{rough}^{TE/TM} = \rho \cdot \Gamma_{smooth}^{TE/TM} = e^{-\frac{g}{2}} \cdot \Gamma_{smooth}^{TE/TM}, \tag{1}$$

where

$$g = \left(\frac{4\pi \cdot \sigma \cdot \cos\theta_i}{\lambda} \right)^2. \tag{2}$$

Here, θ_i is the angle of incidence and reflection, σ the standard deviation of the surface roughness and λ the free space wavelength of the incident wave. The above inherently assumes a Kirchoff approximation whereby the wavelength is assumed to be much less than the mean surface curvature radius, and thus, the surface is locally smooth (i.e., flat). The choice of this classical asymptotic model instead of others to evaluate the field scattered by a random rough surface is founded on its simplicity, and hence, low computational cost, and the fact that the properties of the scenario's surfaces broadly fall within its validity domain [52]. Comparison of the existing different models is beyond the scope of this manuscript. In our implementation, $\Gamma_{rough}^{TE/TM}$ can be enabled independently for any surface in the simulation. The implemented model goes from specular to diffuse scattering, while the in-between regime of observing speckle scattering is not considered. The omission of the non-specular multipath (i.e., incoherent scattering) by nature of the Rayleigh-Rice theory facilitates the comparison with the channel sounding campaign, as the latter naturally filters out the incoherent components due to averaging over hundreds of channel impulse responses.

The molecular absorption effect of water vapor and oxygen is non-negligible in the THz spectrum. Thus, the atmospheric attenuation and dispersion have been considered in the in-house developed 3D-RL algorithm following [53], where the specific gaseous attenuation is given by:

$$\gamma = \gamma_0 + \gamma_w = 0.1820 f (N''_{Oxygen}(f) + N''_{WaterVapour}(f)) \text{ (dB/km)}, \tag{3}$$

where γ_0 and γ_w are the specific attenuation of dry air and water vapor, respectively; f denotes the frequency; and $N''(f)$ is the imaginary part of the complex refractive index for oxygen and water vapour, respectively. Fig. 3 shows the atmospheric attenuation by water and oxygen molecules up to 1 THz. It can be observed that water vapour dominates atmospheric attenuation above 300 GHz. The spectral windows of relative transparency between the absorption resonance peaks are suitable only for short-range communications [2] such as that studied here, and short-range sensing such as automotive radar [30], [54], as attenuation is around 100 dB/km .

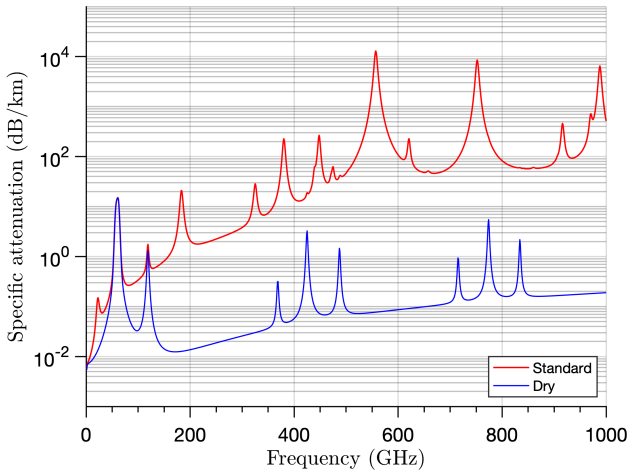

Fig. 3: Atmospheric attenuation implemented in the THz 3D-RL algorithm based on [53]. Water vapour density of 7.5 g/m^3 (Standard) and dry atmosphere (Dry).

B. Channel Measurement Validation

In order to validate the ray launching technique introduced in the previous section, the results of a channel measurement campaign carried out by the Fraunhofer HHI [55] are used. The channel measurement campaign took place in a conference room on the premise of the Fraunhofer HHI in Berlin, Germany, simulating an access point scenario. In total, a number of 8 receiver positions were measured. This section gives an overview of the channel measurement campaign carried out: it includes a description of the channel sounder setup, the measurement scenario, the measurement procedure and the results. Further information on the channel measurement campaign can be found in [55].

1) Channel Sounder Setup: The channel sounder used in this measurement campaign operates at a carrier frequency of 300 GHz with a measurement bandwidth of 2 GHz. The setup is based on the principle of time-domain channel sounding [24] and delivers channel impulse response data. The setup is realised by advanced test and measurement equipment and THz transceiver front ends that were developed within the Fraunhofer Society. The setup can be divided into a stationary transmitter - mainly consisting of a vector signal generator (R&S®SMW200A) and THz transceiver front end - and a mobile receiver - mainly consisting of a vector signal analyzer (R&S®FSW43) and THz transceiver front end.

Table III lists the channel sounder setup's main parameters. Detailed description of the channel sounder setup and especially the THz transceiver front ends can be found in [56].

TABLE III: Parameters of channel sounder setup.

Parameter	Value and unit
Carrier Frequency	300 GHz
Measurement Bandwidth	2 GHz
Resolution in Delay / Angular Domain	0.5 ns / 15°
Transmit / Receive Antenna Gain	6 dBi / 20 dBi
Transmit antenna half-power beamwidth	90° E- / 90° H-plane
Receive antenna half-power beamwidth	15° E-/ 90° H-plane
Sequence Duration / Length in Samples	100 µs / 200000
Number of Snapshots per Angle	500
Correlation- / Averaging- / Processing-Gain	53 dB / 27 dB / 80 dB

2) Measurement Scenario and Procedure: The conference room's dimensions are about 4.7 m by 7.8 m with a ceiling height of about 2.9 m. As typical for conference rooms, the environment is mainly characterised by walls, glass fronts and furniture. Part of the furniture are office chairs, a large wooden table, a TV screen and a whiteboard. To simulate an access point scenario, the transmitter was placed in the corner of the room at a height of 1.86 m and the receiver on several positions on the table at a height about 0.93 m. In this scenario, the transmitter acts as an access point and the receiver as the user equipment (for example a laptop) at several positions.

The receiver (i.e., the front end mounted on the rotation table) was placed on 8 positions on the table, located in the middle of the conference room. At each measurement position, the front end is sequentially rotated in 15° steps, resulting in 24 angles for each measurement position. The angular stepsize corresponds to the receive antenna's half power beamwidth of 15° in the azimuth. At each angle, the receiver samples multiple transmitted sounding sequences, each having a sequence duration of 100 µs. In total 500 sequences are sampled per azimuth angle.

Figure 4 illustrates the channel sounder setup with its components and interconnections in the conference room. Figure 5 shows a photo taken in the conference room while the measurements campaign's execution.

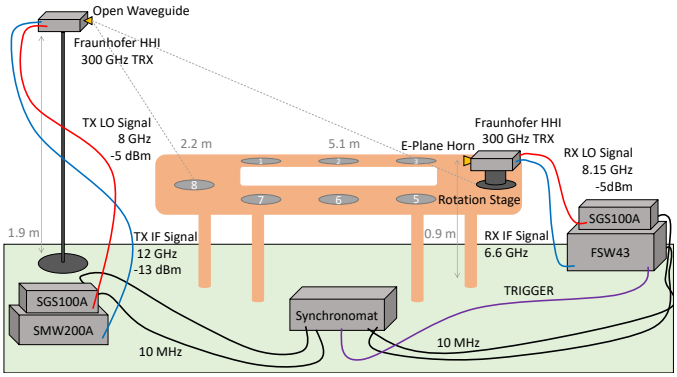

Fig. 4: Illustration of channel sounder setup.

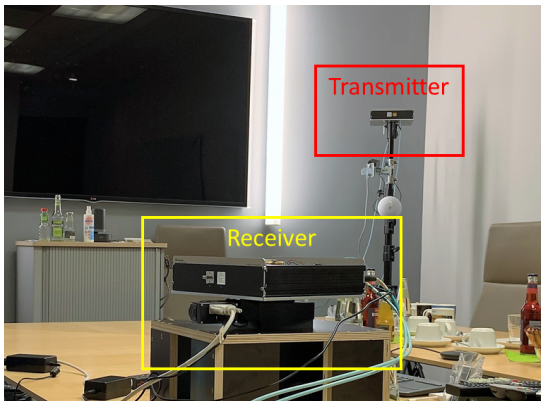

Fig. 5: Photograph of the conference room channel measurement campaign illustrating the channel sounder setup and a section of the conference room. The stationary transmitter and mobile receiver are located on the top right and at the bottom of the figure, respectively.

3) Measurement Evaluation and Results: After the channel measurement campaign, the collected raw measurement data is evaluated in multiple consecutive processing steps, that can be divided into pre-processing, post-processing and multipath component extraction [57]. The outcome of each processing step are channel responses, firstly calibrated, afterwards processed and finally parameterized. Further processing results in channel parameters such as path gain / loss, root mean square (RMS) delay spread (σ_τ) and angular spread (σ_ϕ).

The path gain is calculated by summing up all extracted multipath components' power for each measurement position. Path loss is then derived from path gain by de-embedding the antenna gain for both, transmitter and receiver (26 dBi in total).

The International Telecommunication Union (ITU) describes the RMS delay spread (that accounts for the different arrival times of the multipath-generated copies of the same signal) as the power weighted standard deviation of the excess delays [58]. It is given by the second moment of the power delay profile and provides a measure of the variability of the mean delay. Eq. (4) defines the RMS delay spread σ_τ in dependence of the delay of i-th path τ_i, the power of i-th path $p(\tau_i)$, the delay of the first received multipath component τ_M and the average delay T_D defined in Eq. (5). In line-of-sight (LOS) scenarios, τ_M corresponds to the direct and therefore first path, resulting in $\tau_M = \tau_{i=1}$. Its power $p(\tau_M)$ corresponds to the previously mentioned channel gain.

$$\sigma_\tau = \sqrt{\frac{\sum_{i=1}^{N}(\tau_i - T_D - \tau_M)^2 \; p(\tau_i)}{\sum_{i=1}^{N} p(\tau_i)}} \tag{4}$$

$$T_D = \frac{\sum_{i=1}^{N} \tau_i \; p(\tau_i)}{\sum_{i=1}^{N} p(\tau_i)} - \tau_M \tag{5}$$

Besides delay dispersion, the THz channel also presents angular dispersion caused by the fact that the signal departs from the transmitter to different directions, interact with the different obstacles in the environment, and arrive at the receiver from different directions. The RMS angular spread is defined as the second central moment of the angular power spectrum, in analogy to the RMS delay spread. Based on [59], the RMS angular spread σ_ϕ is calculated as follows:

$$\sigma_\phi = \sqrt{-2\ln\left(\left|\frac{\sum_{n=1}^{N}\sum_{m=1}^{M} \exp(j\Phi_{n,m}) P_{n,m}}{\sum_{n=1}^{N}\sum_{m=1}^{M} P_{n,m}}\right|\right)} \tag{6}$$

where $P_{n,m}$ is the power for the mth subpath of the nth path and $\Phi_{n,m}$ is the subpaths angle given in radians.

Table IV lists the results of the mentioned channel parameters for each measurement position.

TABLE IV: Results of measured channel parameters.

Measurement Position	Path Loss in dB	σ_τ in ns	σ_ϕ in °
1	96.7	7.5	25.5
2	99.0	8.0	25.1
3	98.8	5.5	22.4
4	101.9	1.8	18.8
5	97.6	2.9	17.8
6	101.4	10.6	56.2
7	99.7	6.2	65.4
8	101.2	4.1	28.5

C. Simulation Scenario description

The same scenario of the experimental campaign of measurements has been modelled in the 3D-RL algorithm for simulation and validation purposes. A schematic view of the simulated conference room environment is shown in Fig. 6. All conference room elements described in the previous section (wooden table, office chairs, window, etc.) have been considered with the characterized electromagnetic material properties at 300 GHz presented in Table II, and reproduced again in Table V to single out the set of materials used in the specific office scenario, along with the standard deviation of the roughness σ. The conductivity of aluminium is taken from [60]. Note that the tabulated data in Table V has not been extracted from conference room samples, but from materials of similar nature and some difference may exist. Such difference, if any, is arguably small given the analysis in terms of categories (wood, tile, stone, leather, fabric and plastic) reported in [61] and will have no impact in the results. Founded on the literature [12], the roughness correlation length of the surfaces has been assumed to be larger than the wavelength, so Kirchoff theory is valid [62]. The spheres in the figure are shown for illustration purposes and represent the positions of the transmitter (yellow sphere), and the different measurement points just above the table (red spheres) in the considered scenario.

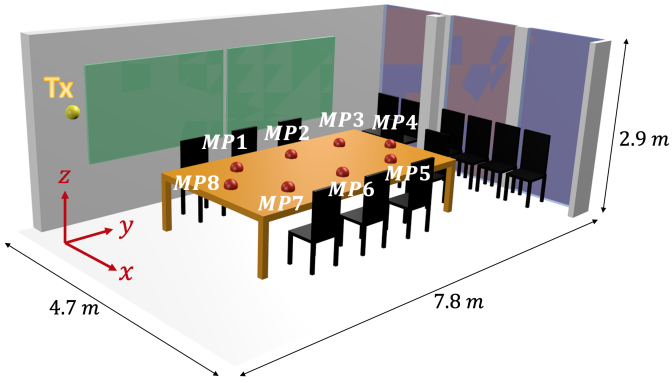

Fig. 6: Schematic view of the conference room simulated scenario. Ceiling has been hidden for illustration purposes.

TABLE V: Materials and their associated dielectric and surface roughness properties for simulation.

Material	ε_r	ε_i	σ (mm)
Aluminum	-3.3×10^4	2.2×10^6	0.00024 [60]
Aniline Leather	1.771	0.069	0.049 [63]
Antique Pine	2.148	0.235	0.0468 [64]
Balsa	1.527	0.069	0.047 [64]
Brick	4.478	0.604	0.095 [63]
Glass	3.956	0.264	0.014 [19]
Plywood	2.037	0.120	0.0468 [64]
Polypropylene	2.319	0.0005	0.075 [19]
uPVC	1.522	0.025	0.075 [19]

IV. Results and Discussion

In order to validate the diffuse-scattering-informed 3D-RL algorithm, the simulation settings correspond to the experi-

mental measurement parameter setup, including the radiation patterns of the transmitter and receiver antennas. Besides, a calibration analysis in terms of number of reflections is initially carried out. This algorithm calibration process has consisted of carrying out several simulations where the number of reflections considered has been modified. Then, path loss, RMS delay spread and angular spread have been cross-correlated with measurements at the point positions (MP1 to MP8) when the algorithm does and does not incorporate scattering loss. This preliminary analysis helps assessing not only the impact of scattering loss, but also the impact of multipath propagation in the considered scenario at a frequency where LOS components become more dominant than at microwave frequencies [65].

Table VI presents the average of the absolute mean error between simulation and measurements for increasing number of considered reflections for the 8 measurement positions. The differences seen in path loss, RMS delay spread and RMS angular spread as a function of considered reflections is significantly lower than those seen at microwave frequencies [25], [66], which highlights the dominance of the LOS path at THz frequencies as anticipated in previous studies when computing the K-factor values [65]. Simulations converge toward measurements when considering four reflections and scattering loss is enabled in the algorithm. Specifically, the mean absolute error for path loss, RMS delay spread and RMS angular spread is 0.77 dB, 0.94 ns, and 2.07 °, respectively. Disabling the scattering loss in the simulations leads to higher absolute mean error in all analyzed channel model parameters. This partial analysis suggests the importance of considering the material roughness at these frequency bands, showing that scattering objects in a scene can have a huge bearing on scattered energy. From now on, all reported results are obtained with a reflection depth of four bounces.

TABLE VI: Simulation vs measurements absolute mean error comparison.

Reflections	**Path Loss in dB**		σ_τ **in ns**		σ_ϕ **in °**	
Scattering	✓[a]	✗[b]	✓	✗	✓	✗
1 ref.	6.17	7.61	3.16	3.46	27.47	31.63
2 ref.	7.45	8.33	2.87	3.11	35.94	36.58
3 ref.	5.63	6.02	2.82	2.95	22.04	23.19
4 ref.	0.77	4.39	0.94	2.47	2.07	7.54

[a] Scattering enabled.
[b] Scattering disabled.

Figures 7, 8 and 9 show the comparison between simulation (with and without scattering loss) and experimental measurement results for each point for the channel parameters path gain, RMS delay spread and angular spread, respectively. As anticipated from the tabulated results in Table VI, simulation and measurement results achieve better agreement when scattering phenomenon is enabled in the 3D-RL algorithm, reinforcing that scattering matters and it can not be neglected when modeling the physical channel parameters at THz frequencies. To some extend, these results also show that the control over the individual materials considered and a precise THz materials properties characterization is crucial to obtaining accurate results from the simulation, ensuring that each structure best represents the real-world properties of the scene. We have confirmed this quantitatively somewhere else [61].

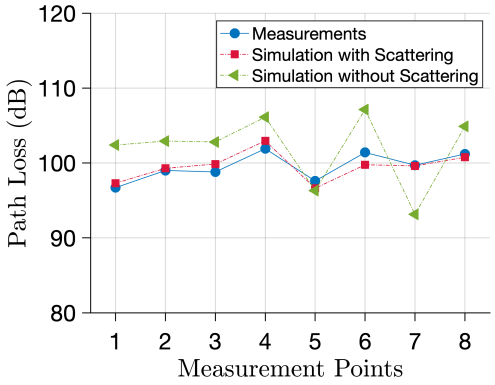

Fig. 7: Simulation and measurements Path Loss results comparison for MP1 to MP8.

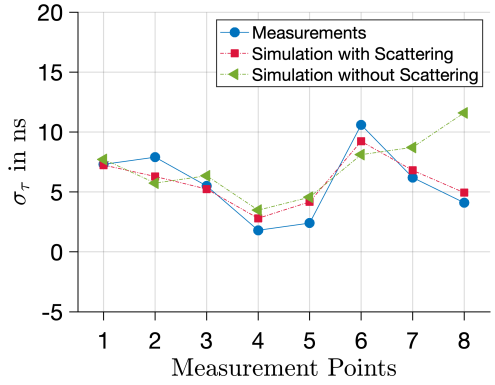

Fig. 8: Simulation and measurements σ_τ results comparison for MP1 to MP8.

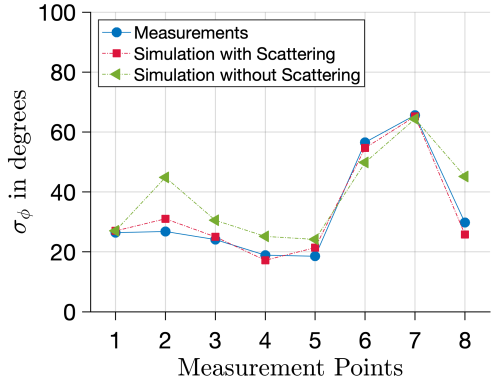

Fig. 9: Simulation and measurements σ_ϕ results comparison for MP1 to MP8.

Once the validation of the THz module has been performed at the point positions MP1 to MP8, results for the complete

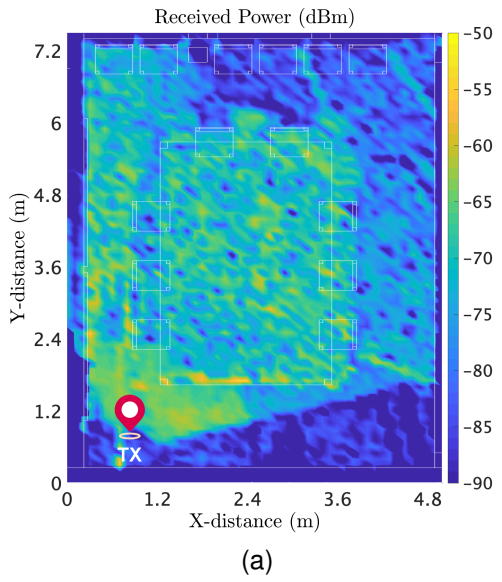

Fig. 10: Received Power at 0.93 m height (see Fig. 6 for reference), (a) With scattering. (b) Without scattering. (c) CDF received power comparison with and without scattering consideration.

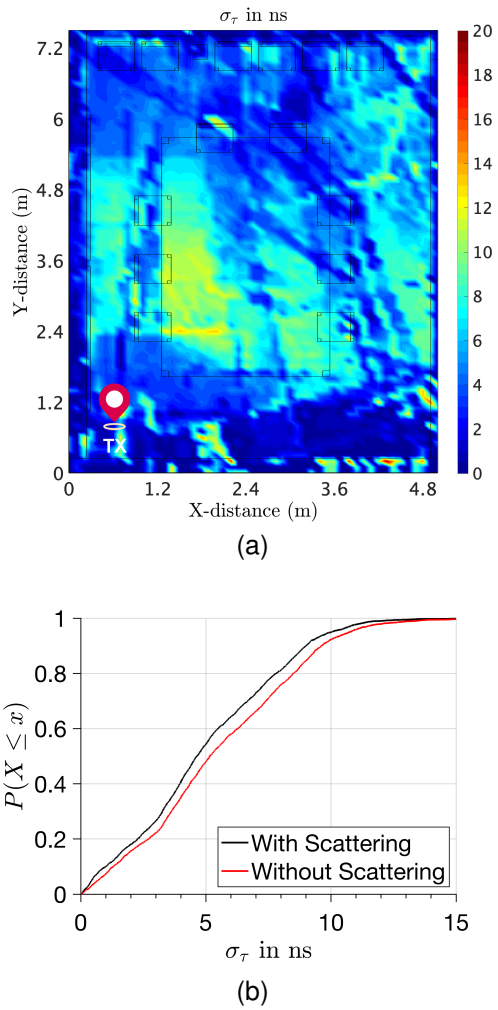

Fig. 11: (a) XY bi-dimensional σ_τ plane with scattering at 0.93 m height (see Fig. 6 for reference), (b) CDF σ_τ comparison with and without scattering consideration for the table top plane.

analyzed volumetric scenario can be obtained efficiently, unlike measurements. In particular, we report next the received power spatial distribution at the table top plane (0.93 m) when scattering loss is and is not accounted for, see Fig. 10a and Fig. 10b, respectively. The cross-correlation of both panels reveals the radiation pattern of the transmitter antenna in the lower left corner and the rapid loss of coherence when scattering loss is implemented. The latter is more evident in the centre of the table and on the top right-hand side corner of the figure where the interference pattern diminishes and falls below noise level at some points, respectively. The mean absolute difference between Fig. 10a and Fig. 10b is 5.85 dB. In addition, Fig. 10c depicts the cumulative distribution function (CDF) of received power for both planes, showing the higher losses when scattering is enabled.

In order to gain further insight on the multipath propagation effect, the channel parameter σ_τ again on the table top plane is displayed in Fig. 11a, whereas the CDF of σ_τ with scattering loss enabled and disabled in the simulation is displayed in Fig. 11b. We plot the cumulative distribution

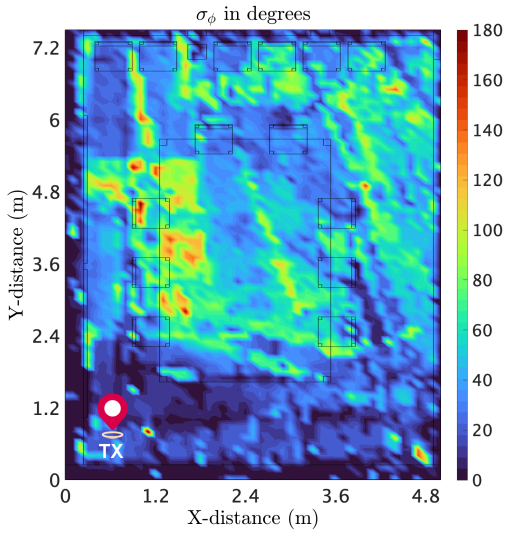

(a)

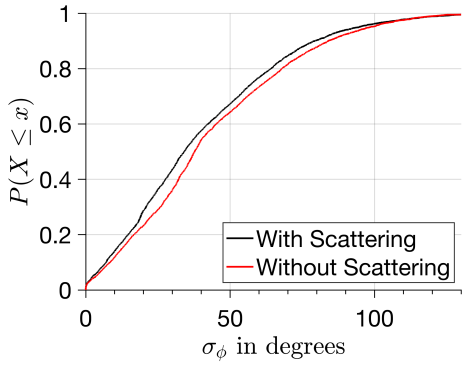

(b)

Fig. 12: (a) XY bi-dimensional σ_ϕ plane with scattering at 0.93 m height (see Fig. 6 for reference), (b) CDF σ_ϕ comparison with and without scattering consideration for the table top plane.

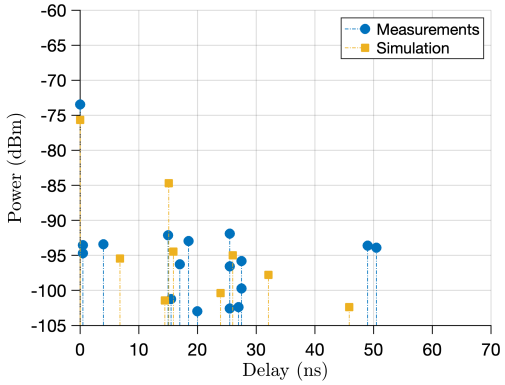

Fig. 13: Power delay profile comparison at MP2 (see Fig. 6 for reference).

function rather than the received signal level against time delay at specific points to be able to extract general conclusions about the scenario. From Fig. 11a, it can be seen that the inclusion of finer detail in the model is essential, as THz electromagnetic interactions require the inclusion of every single small structure given the THz wavelength. Meanwhile, Fig. 11b shows that σ_τ has lower values when scattering is considered in the algorithm. This is a natural consequence of the rapidly diminishing contribution of multipath components due to cumulative scattering loss (as described in Eq. 1 for a single event) upon multiple bounces on rough surfaces.

Finally, Fig. 12 presents results associated to the channel parameter σ_ϕ for the table top plane: Fig. 12a shows the impact of the scenario scatterers in σ_ϕ, and Fig. 12b shows the CDF of σ_ϕ with scattering phenomenon enabled and disabled in the simulation algorithm. Akin to σ_τ, Fig. 12a, demonstrates the crucial impact of finer detail of the scene on σ_ϕ for 300 GHz, whereas Fig. 12b shows the reduction in σ_ϕ because of the scattering loss induced rapidly diminishing contribution of multipath components. In addition, as an example, Fig. 13 shows the corresponding power delay profile comparison between simulation and measurements for MP2 (see Fig. 6 for reference), showing a good agreement between them.

In summary, all the above results demonstrate (and quantify for the first time) that the inclusion of diffuse scattering along with precise material properties considerations (further investigation on the impact of material properties can be found elsewhere [61]) are pivotal at THz frequency bands for accurate propagation planning of real-world environments.

V. Conclusions

In this paper, a deterministic channel model approach for propagation planning at THz frequency bands is presented and validated experimentally. This tool includes a THz electromagnetic material properties library of 27 common building and office materials, which has been built up based on experimental measurements with a THz time-domain-spectroscopy system. The algorithm incorporates scattering loss from rough surfaces and atmospheric attenuation at these frequency bands. In order to validate the proposed algorithm, a channel sounder measurement campaign has been performed in a typical indoor environment at 300 GHz frequency band, showing good agreement between them. The impact of considering scattering by rough surfaces in the simulation is presented, demonstrating the need to account for this phenomenon in the THz band. These results and the proposed geometric channel modeling technique lay the foundation to design reliable and efficient communication systems in the THz Band.

Acknowledgments

The authors would like to thank Ajla Nekovic, Emily Adams, Toby Attwood, Christopher Sumner, Morgan Dryhurst and Suzanna Freer for supporting the material database creation.

References

[1] T. Kürner, D. M. Mittleman, and T. Nagatsuma, *THz Communications: Paving the Way Towards Wireless Tbps*, ser. Springer Series in Optical Sciences, T. Kürner, D. M. Mittleman, and T. Nagatsuma, Eds. Springer International Publishing, 2022, vol. 234.

[2] D. Serghiou, M. Khalily, T. W. Brown, and R. Tafazolli, "Terahertz Channel Propagation Phenomena, Measurement Techniques and Modeling for 6G Wireless Communication Applications: A Survey, Open Challenges and Future Research Directions," *IEEE Communications Surveys & Tutorials*, vol. 24, no. 4, pp. 1957–1996, 2022.

[3] C. Han, Y. Wang, Y. Li, Y. Chen, N. A. Abbasi, T. Kürner, and A. F. Molisch, "Terahertz Wireless Channels: A Holistic Survey on Measurement, Modeling, and Analysis," *IEEE Communications Surveys & Tutorials*, vol. 24, no. 3, pp. 1670–1707, 2022.

[4] G. Carpintero, E. García-Muñoz, H. Hartnagel, S. Preu, and A. Raisanen, *Semiconductor TeraHertz Technology: Devices and Systems at Room Temperature Operation*, ser. IEEE Press. Chichester, U.K.: Wiley, 2015.

[5] D. He, K. Guan, A. Fricke, B. Ai, R. He, Z. Zhong, A. Kasamatsu, I. Hosako, and T. Kurner, "Stochastic Channel Modeling for Kiosk Applications in the Terahertz Band," *IEEE Transactions on Terahertz Science and Technology*, vol. 7, no. 5, pp. 502–513, 2017.

[6] S. Priebe and T. Kurner, "Stochastic Modeling of THz Indoor Radio Channels," *IEEE Transactions on Wireless Communications*, vol. 12, no. 9, pp. 4445–4455, 2013.

[7] S. Priebe, M. Jacob, and T. Kuerner, "AoA, AoD and ToA Characteristics of Scattered Multipath Clusters for THz Indoor Channel Modeling," in *17th European Wireless 2011 - Sustainable Wireless Technologies*, 2011, pp. 1–9.

[8] S. Priebe, M. Kannicht, M. Jacob, and T. Kurner, "Ultra broadband indoor channel measurements and calibrated ray tracing propagation modeling at THz frequencies," *Journal of Communications and Networks*, vol. 15, no. 6, pp. 547–558, 2013.

[9] J. Wang, C.-X. Wang, J. Huang, H. Wang, X. Gao, X. You, and Y. Hao, "A Novel 3D Non-Stationary GBSM for 6G THz Ultra-Massive MIMO Wireless Systems," *IEEE Transactions on Vehicular Technology*, vol. 70, no. 12, pp. 12 312–12 324, 2021.

[10] S. Kim and A. G. Zajić, "Statistical Characterization of 300-GHz Propagation on a Desktop," *IEEE Transactions on Vehicular Technology*, vol. 64, no. 8, pp. 3330–3338, 2015.

[11] C. Han, A. O. Bicen, and I. F. Akyildiz, "Multi-ray channel modeling and wideband characterization for wireless communications in the terahertz band," *IEEE Transactions on Wireless Communications*, vol. 14, no. 5, pp. 2402–2412, 2015.

[12] C. Jansen, S. Priebe, C. Moller, M. Jacob, H. Dierke, M. Koch, and T. Kurner, "Diffuse scattering from rough surfaces in THz communication channels," *IEEE Transactions on Terahertz Science and Technology*, vol. 1, no. 2, pp. 462–472, 2011.

[13] D. Cahyono, F. Sheikh, and T. K. Ser, "Deterministic Approach of Indoor Room THz Multipath Channel Model," *2020 8th International Conference on Information and Communication Technology, ICoICT 2020*, pp. 5–9, 2020.

[14] H. Yi, K. Guan, D. He, B. Ai, J. Dou, and J. Kim, "Characterization for the Vehicle-to-Infrastructure Channel in Urban and Highway Scenarios at the Terahertz Band," *IEEE Access*, vol. 7, pp. 166 984–166 996, 2019.

[15] V. Degli-Esposti, F. Fuschini, E. M. Vitucci, and G. Falciasecca, "Measurement and Modelling of Scattering From Buildings," *IEEE Transactions on Antennas and Propagation*, vol. 55, no. 1, pp. 143–153, 2007.

[16] K. Guan, B. Peng, D. He, J. M. Eckhardt, S. Rey, B. Ai, Z. Zhong, and T. Kürner, "Measurement, Simulation, and Characterization of Train-to-Infrastructure Inside-Station Channel at the Terahertz Band," *IEEE Transactions on Terahertz Science and Technology*, vol. 9, no. 3, pp. 291–306, 2019.

[17] F. Sheikh, Y. Gao, and T. Kaiser, "A Study of Diffuse Scattering in Massive MIMO Channels at Terahertz Frequencies," *IEEE Transactions on Antennas and Propagation*, vol. 68, no. 2, pp. 997–1008, 2020.

[18] R. Piesiewicz, T. Kleine-Ostmann, N. Krumbholz, D. Mittleman, M. Koch, and T. Kürner, "Terahertz characterisation of building materials," *Electron. Lett.*, vol. 41, no. 18, pp. 1002–1004, 2005.

[19] R. Piesiewicz, C. Jansen, S. Wietzke, D. Mittleman, M. Koch, and T. Kürner, "Properties of building and plastic materials in the THz range," *Int. J. Infr. Millim. Waves*, vol. 28, no. 5, pp. 363–371, 2007.

[20] R. Piesiewicz, C. Jansen, D. Mittleman, T. Kleine-Ostmann, M. Koch, and T. Kürner, "Scattering Analysis for the Modeling of THz Communication Systems," *IEEE Transactions on Antennas and Propagation*, vol. 55, no. 11, pp. 3002–3009, 2007.

[21] K. Yee, "Numerical solution of initial boundary value problems involving Maxwell's equations in isotropic media," *IEEE Transactions on Antennas and Propagation*, vol. 14, no. 3, pp. 302–307, 1966.

[22] Y. Zhao, Y. Hao, and C. Parini, "FDTD Characterization of UWB Indoor Radio Channel Including Frequency Dependent Antenna Directivities," *IEEE Antennas and Wireless Propagation Letters*, vol. 6, pp. 191–194, 2007.

[23] A. Taflove and S. C. Hagness, *Computational Electrodynamics: The Finite-Difference Time-Domain Method*. Boston, MA, USA: Artech House, 2005.

[24] A. F. Molisch, *Wireless Communications, 2nd ed.*, ser. IEEE Press. Chichester, U.K.: Wiley, 2011.

[25] L. Azpilicueta, M. Rawat, K. Rawat, F. M. Ghannouchi, and F. Falcone, "A Ray Launching-Neural Network Approach for Radio Wave Propagation Analysis in Complex Indoor Environments," *IEEE Transactions on Antennas and Propagation*, vol. 62, no. 5, pp. 2777–2786, 2014.

[26] L. Azpilicueta, F. Falcone, and R. Janaswamy, "A Hybrid Ray Launching-Diffusion Equation Approach for Propagation Prediction in Complex Indoor Environments," *IEEE Antennas and Wireless Propagation Letters*, vol. 16, pp. 214–217, 2017.

[27] ITU-R, "Effects of building materials and structures on radiowave propagation above about 100 MHz P Series Radiowave propagation," *Recommendation ITU-R P.2040*, vol. 1, 2013. [Online]. Available: http://www.itu.int/rec/R-REC-P.2040-0-201309-I

[28] M. Scheller, C. Jansen, and M. Koch, "Analyzing sub-100-μm samples with transmission terahertz time domain spectroscopy," *Optics Communications*, vol. 282, no. 7, pp. 1304–1306, 2009.

[29] M. Ma, Y. Wang, M. Navarro-Cía, F. Liu, F. Zhang, Z. Liu, Y. Li, S. M. Hanham, and Z. Hao, "The dielectric properties of some ceramic substrate materials at terahertz frequencies," *Journal of the European Ceramic Society*, vol. 39, no. 14, pp. 4424–4428, 2019.

[30] S. M. Sabery, A. Bystrov, M. Navarro-Cía, P. Gardner, and M. Gashinova, "Study of low terahertz radar signal backscattering for surface identification," *Sensors*, vol. 21, no. 9, p. 2954, 2021.

[31] S. Freer, A. Gorodetsky, and M. Navarro-Cía, "Beam Profiling of a Commercial Lens-Assisted Terahertz Time Domain Spectrometer," *IEEE Transactions on Terahertz Science and Technology*, vol. 11, no. 1, pp. 90–100, 2021.

[32] E. Adams, T. Attwood, S. Freer, S. M. Hanham, C. Constantinou, F. Hu, L. Azpilicueta, and M. Navarro-Cía, "Broadband Characterisation of Interior Materials and Surface Scattering using Terahertz Time-Domain Spectroscopy," in *2021 14th UK-Europe-China Workshop on Millimetre-Waves and Terahertz Technologies (UCMMT)*, 2021, pp. 1–3.

[33] S. Freer, C. Sui, S. M. Hanham, L. M. Grover, and M. Navarro-Cía, "Hybrid reflection retrieval method for terahertz dielectric imaging of human bone," *Biomedical Optics Express*, vol. 12, no. 8, pp. 4807–4820, 2021.

[34] K. H. Breeden and A. P. Sheppard, "A Note on the Millimeter and Submillimeter Wave Dielectric Constant and Loss Tangent Value of Some Common Materials," *Radio Science*, vol. 3, no. 2, pp. 205–205, 1968.

[35] P. Goldsmith, *Quasioptical Systems: Gaussian Beam Quasioptical Propogation and Applications*, ser. IEEE Press Series on RF and Microwave Technology. Wiley, 1998.

[36] D. Han, H. Jo, and J. Ahn, "Terahertz spectroscopy of natural stone materials," in *2014 39th International Conference on Infrared, Millimeter, and Terahertz waves (IRMMW-THz)*, 2014, pp. 1–2.

[37] K. Krügener, S. Sommer, E. Stübling, R. Jachim, M. Koch, and W. Viöl, "THz Properties of Typical Woods Important for European Forestry," *Journal of Infrared, Millimeter, and Terahertz Waves*, vol. 40, no. 7, pp. 770–774, 2019.

[38] T. Otim, P. Lopez-Iturri, L. Azpilicueta, A. Bahillo, L. E. Díez, and F. Falcone, "A 3D Ray Launching Time-Frequency Channel Modeling Approach for UWB Ranging Applications," *IEEE Access*, vol. 8, pp. 97 321–97 334, 2020.

[39] F. Granda, L. Azpilicueta, M. Celaya-Echarri, P. Lopez-Iturri, C. Vargas-Rosales, and F. Falcone, "Spatial V2X Traffic Density Channel Characterization for Urban Environments," *IEEE Transactions on Intelligent Transportation Systems*, vol. 22, no. 5, pp. 2761–2774, 2021.

[40] L. Azpilicueta, C. Vargas-Rosales, and F. Falcone, "Intelligent Vehicle Communication: Deterministic Propagation Prediction in Transportation Systems," *IEEE Vehicular Technology Magazine*, vol. 11, no. 3, pp. 29–37, 2016.

[41] L. Azpilicueta, J. J. Astrain, P. Lopez-Iturri, F. Granda, C. Vargas-Rosales, J. Villadangos, A. Perallos, A. Bahillo, and F. Falcone, "Optimization and Design of Wireless Systems for the Implementation of Context Aware Scenarios in Railway Passenger Vehicles," *IEEE Transactions on Intelligent Transportation Systems*, vol. 18, no. 10, pp. 2838–2850, 2017.

[42] L. Azpilicueta, P. López Iturri, E. Aguirre, J. J. Astrain, J. Villadangos, C. Zubiri, and F. Falcone, "Characterization of Wireless Channel

Impact on Wireless Sensor Network Performance in Public Transportation Buses," *IEEE Transactions on Intelligent Transportation Systems*, vol. 16, no. 6, pp. 3280–3293, 2015.

[43] F. A. Rodríguez-Corbo, L. Azpilicueta, M. Celaya-Echarri, P. Lopez-Iturri, A. V. Alejos, R. M. Shubair, and F. Falcone, "Deterministic and Empirical Approach for Millimeter-Wave Complex Outdoor Smart Parking Solution Deployments," *Sensors*, vol. 21, no. 12, p. 4112, 2021.

[44] M. Celaya-Echarri, L. Azpilicueta, P. Lopez-Iturri, F. Falcone, M. Garcia Sanchez, and A. Vazquez Alejos, "Validation of 3D simulation tool for radio channel modeling at 60 GHz: A meeting point for empirical and simulation-based models," *Measurement*, vol. 163, p. 108038, 2020.

[45] L. Azpilicueta, P. Lopez-Iturri, J. Zuñiga-Mejia, M. Celaya-Echarri, F. A. Rodríguez-Corbo, C. Vargas-Rosales, E. Aguirre, D. G. Michelson, and F. Falcone, "Fifth-Generation (5G) mmWave Spatial Channel Characterization for Urban Environments' System Analysis," *Sensors*, vol. 20, no. 18, 2020.

[46] F. A. Rodríguez-Corbo, L. Azpilicueta, M. Celaya-Echarri, P. Lopez-Iturri, I. Picallo, F. Falcone, and A. V. Alejos, "Deterministic 3D Ray-Launching Millimeter Wave Channel Characterization for Vehicular Communications in Urban Environments," *Sensors*, vol. 20, no. 18, p. 5284, 2020.

[47] L. Azpilicueta, F. Falcone, and R. Janaswamy, "Hybrid Computational Techniques: Electromagnetic Propagation Analysis in Complex Indoor Environments," *IEEE Antennas and Propagation Magazine*, vol. 61, no. 6, pp. 20–30, 2019.

[48] F. Casino, L. Azpilicueta, P. Lopez-Iturri, E. Aguirre, F. Falcone, and A. Solanas, "Optimized Wireless Channel Characterization in Large Complex Environments by Hybrid Ray Launching-Collaborative Filtering Approach," *IEEE Antennas and Wireless Propagation Letters*, vol. 16, pp. 780–783, 2017.

[49] F. Casino, P. Lopez-Iturri, E. Aguirre, L. Azpilicueta, F. Falcone, and A. Solanas, "Enhanced Wireless Channel Estimation Through Parametric Optimization of Hybrid Ray Launching-Collaborative Filtering Technique," *IEEE Access*, vol. 8, pp. 83 070–83 080, 2020.

[50] H. Ragheb and E. R. Hancock, "The modified Beckmann–Kirchhoff scattering theory for rough surface analysis," *Pattern Recognition*, vol. 40, no. 7, pp. 2004–2020, 2007.

[51] J. C. Stover, *Optical Scattering: Measurement and Analysis, 3rd ed.* Bellingham, Washington, USA: SPIE Press, 2012.

[52] N. Pinel and C. Bourlier, *Electromagnetic wave scattering from random rough surfaces - Asymptotic models.*, ser. FOCUS SERIES in WAVES. London, UK: ISTE - Wiley, 2013.

[53] ITU-R, "Attenuation by atmospheric gases and related effects P Series Radiowave propagation," *Recommendation ITU-R P.676-13*, vol. 1, 2022. [Online]. Available: https://www.itu.int/rec/R-REC-P.676-13-202208-I/en

[54] L. Daniel, A. Stove, E. Hoare, D. Phippen, M. Cherniakov, B. Mulgrew, and M. Gashinova, "Application of Doppler beam sharpening for azimuth refinement in prospective low-THz automotive radars," *IET Radar, Sonar & Navigation*, vol. 12, no. 10, pp. 1121–1130, 2018.

[55] A. Schultze, F. Undi, M. Peter, W. Keusgen, and T. Eichler, "Angle-Resolved THz Channel Measurements at 300 GHz in a Conference Room Environment," in *2021 XXXIVth General Assembly and Scientific Symposium of the International Union of Radio Science (URSI GASS)*, 2021, pp. 1–4.

[56] M. Schmieder, W. Keusgen, M. Peter, S. Wittig, T. Merkle, S. Wagner, M. Kuri, and T. Eichler, "THz Channel Sounding: Design and Validation of a High Performance Channel Sounder at 300 GHz," in *2020 IEEE Wireless Communications and Networking Conference Workshops (WCNCW)*, 2020, pp. 1–6.

[57] S. Wittig, M. Peter, and W. Keusgen, "A Reference Model for Channel Sounder Performance Evaluation, Validation and Comparison," in *2022 16th European Conference on Antennas and Propagation (EuCAP)*, 2022, pp. 1–5.

[58] ITU-R, "Multipath propagation and parameterization of its characteristics," in *Recommendation ITU-R P.1407-8*. ITU, 2021, pp. 1–34.

[59] ETSI, "Study on channel model for frequencies from 0.5 to 100 GHz," in *3GPP TR 38.901 version 17.0.0 Release 17*. 3GPP, 2022.

[60] M. Naftaly, *Terahertz Metrology*. Artech House, 2015.

[61] L. Azpilicueta, A. Schulze, M. Celaya-Echarri, F. A. Rodríguez-Corbo, C. Sumner, M. Dryhurst, R. M. Shubair, F. Falcone, and M. Navarro-Cía, "TeraHertz vs Microwaves Ray-Launching Model in a 0.45 THz Indoor Wireless Scenario," in *2023 48th International Conference on Infrared, Millimeter and Terahertz Waves (IRMMW-THz)*, 2023, pp. 1–2.

[62] R. Vaughan and J. Bach-Anderson, *Channels, Propagation and Antennas for Mobile Communications*, ser. Electromagnetic Waves. Institution of Engineering and Technology, 2003.

[63] M. Alissa, B. Friederich, F. Sheikh, A. Czylwik, and T. Kaiser, "Experimental Investigation of Terahertz Scattering: A Study of Non-Gaussianity and Lateral Roughness Influence," *IEEE Access*, vol. 8, pp. 170 672–170 680, 2020.

[64] F. Sheikh, Y. Zantah, I. Ben Mabrouk, M. Alissa, J. Barowski, I. Rolfes, and T. Kaiser, "Scattering and Roughness Analysis of Indoor Materials at Frequencies from 750 GHz to 1.1 THz," *IEEE Transactions on Antennas and Propagation*, vol. 69, no. 11, pp. 7820–7829, 2021.

[65] A. A. Glazunov, A. Razavi, R. Maaskant, and J. Yang, "Semi-analytical model of the Rician k-factor," *Radio Science*, vol. 55, no. 11, pp. 1–13, 2020.

[66] S. Salous, *Radio Propagation Measurement and Channel Modelling*. John Wiley & Sons, Ltd, 2013.